SI APPENDIX FOR:

How van der Waals interactions determine the unique properties of water

Tobias Morawietz,[1, a)] Andreas Singraber,[2] Christoph Dellago,[2] and Jörg Behler[1, b)]

[1)] *Lehrstuhl für Theoretische Chemie, Ruhr-Universität Bochum, D-44780 Bochum, Germany.*

[2)] *Faculty of Physics, University of Vienna, Sensengasse 8/9, A-1090, Vienna, Austria.*

CONTENTS

a) Electronic mail: tobias.morawietz@theochem.ruhr-uni-bochum.de

b) Electronic mail: joerg.behler@theochem.ruhr-uni-bochum.de

I. SI TEXT

A. Neural Network Potentials for Bulk Water

Ab initio-quality neural network potentials (NNPs) for water were constructed based on the high-dimensional NNP approach by Behler and Parrinello[1]. In this method, the total energy E is written as a sum of atomic energy contributions $E^{\text{hydrogen/oxygen}}$,

$$E = \sum_{i=1}^{N^{\text{hydrogen}}} E_i^{\text{hydrogen}} + \sum_{j=1}^{N^{\text{oxygen}}} E_j^{\text{oxygen}}, \qquad (1)$$

which are expressed by artificial neural networks and depend on the local chemical environment represented by a set of atom-centered symmetry functions[2].

High-dimensional NNPs enable constructing highly accurate and full-dimensional representations of reference potential-energy surfaces for periodic and non-periodic systems[3]. While to date this method has been primarily applied to solid state systems[3], recently high-dimensional NNPs have been employed to describe water clusters in the gas phase[4], and the interaction between water molecules and bimetallic nanoparticles[5]. The present work represents the first construction of NNPs for a condensed molecular system.

We developed a set of four NNPs trained to energies and forces from reference DFT calculations for a broad range of condensed water configurations employing the RPBE[6] and BLYP[7,8] density-functionals with and without vdW corrections. All DFT calculations were carried out with the all-electron code FHI-aims[9] which uses numerical atom-centered orbitals as basis functions. Since it has been shown that AIMD simulations with underconverged basis sets yield underestimated water densities[10], we carefully checked the convergence of our DFT calculations with respect to basis set size (see Fig. S1). For the chosen "*tier* 2" basis set, binding energies, forces, and pressure tensors are well converged, with remaining errors below 4 meV/H$_2$O, 2 meV/Å, and 1.0 %, respectively.

VdW interactions were taken into account by Grimme's D3 method[11] using the zero-damping scheme and neglecting three-body contributions since their effect on the properties of water is negligible[12]. Within the D3 approach, computing the vdW correction term for periodic structures is computationally more demanding than the evaluation of the NNPs. Therefore, vdW energies and forces were added to the reference data before training the NNPs (in contrast to previously developed NNPs for water clusters[4] where vdW interactions were computed on-the-fly in the application of the potentials).

The NNPs were trained using the code RuNNer[13]. All NNPs consist of a set of feed-forward neural networks with two hidden layers containing 25 nodes each, corresponding to a total number of 2,827 parameters per NNP. For the nodes in the hidden layers the hyperbolic tangent was used as activation function, while for the node in the output layer a linear function was used. Local chemical environments were described by symmetry functions of type 2 and type 4[2]. The radial extension of each symmetry function is restricted by a cutoff function f_c that ensures that value and slope become zero at the cutoff radius r_c,

$$f_c(r_{ij}) = \begin{cases} \tanh^3\left[1 - \frac{r_{ij}}{r_c}\right] & \text{with} \quad r_{ij} \leq r_c \\ 0 & \text{with} \quad r_{ij} > r_c. \end{cases} \qquad (2)$$

Here, r_{ij} is the distance between atoms i and j. Radial symmetry functions of type 2 consist of a sum of distance dependent Gaussian functions multiplied by the cutoff function,

$$G_i^2 = \sum_{j \neq i} e^{-\eta(r_{ij} - r_s)^2} f_c(r_{ij}). \qquad (3)$$

Here, the center of the Gaussian can be shifted by the parameter r_s and the parameter η can be adjusted in order to change the Gaussian width. The angular symmetry function of type 4 consists of an angular term that depends on the angle α_{ijk} (centered at atom i and formed with neighbors j and k) and can be adjusted by varying the parameters λ and ζ. Additional terms that depend on the interatomic distances of atoms i, j, and k control the radial resolution,

$$G_i^4 = 2^{1-\zeta} \sum_{j \neq i} \sum_{k \neq i,j} \left[\left(1 + \lambda cos(\alpha_{ijk})\right)^\zeta \right. \qquad (4)$$
$$\left. \times e^{-\eta(r_{ij}^2 + r_{ik}^2 + r_{jk}^2)} f_c(r_{ij}) f_c(r_{ik}) f_c(r_{jk}) \right].$$

A total of 27 and 30 symmetry functions were used to describe the atomic environments of hydrogen and oxygen atoms, respectively. The parameters of the symmetry functions are listed in Tables S1 and S2.

The functional form of the atomic neural networks describing hydrogen and oxygen atoms is then given by,

$$E^{\text{hydrogen}} = f_1^3 \left(b_1^3 + \sum_{k=1}^{25} a_{k1}^{23} f_k^2 \left(b_k^2 + \sum_{j=1}^{25} a_{jk}^{12} \right. \right. \qquad (5)$$
$$\left. \left. \times f_j^1 \left(b_j^1 + \sum_{i=1}^{27} a_{ij}^{01} G_i \right) \right) \right),$$

and,

$$E^{\text{oxygen}} = f_1^3 \left(b_1^3 + \sum_{k=1}^{25} a_{k1}^{23} f_k^2 \left(b_k^2 + \sum_{j=1}^{25} a_{jk}^{12} \right. \right. \qquad (6)$$
$$\left. \left. \times f_j^1 \left(b_j^1 + \sum_{i=1}^{30} a_{ij}^{01} G_i \right) \right) \right),$$

respectively. Here, the weight parameters a_{ij}^{kl} together with the bias weights b_j^i are the fitting parameters of the

NNP and f^1, f^2, and f^3 are activation functions with the following functional form:

$$f^1(x) = \tanh(x), \tag{7}$$

$$f^2(x) = \tanh(x), \tag{8}$$

$$f^3(x) = x. \tag{9}$$

The force component F_{α_k} acting on atom k in direction $\alpha = x$, y, or z, given by the negative gradient of the energy with respect to α_k, is obtained from,

$$F_{\alpha_k} = -\frac{\partial E}{\partial \alpha_k} = -\sum_{i=1}^{N} \frac{\partial E_i}{\partial \alpha_k} = -\sum_{i=1}^{N} \sum_{j=1}^{M_i} \frac{\partial E_i}{\partial G_{i,j}} \frac{\partial G_{i,j}}{\partial \alpha_k}, \tag{10}$$

where the derivatives $\partial E_i / \partial G_{i,j}$ and $\partial G_{i,j} / \partial \alpha_k$ are defined by the functional form of the atomic neural networks and the symmetry functions, respectively. Here, N is the number of atoms and M_i the number of symmetry functions of atom i.

In order to avoid a saturation of the activation functions in the first hidden layer, the initial symmetry function values G_i^0 are always centered and rescaled,

$$G_i = \frac{G_i^0 - G_{i,\text{average}}^0}{G_{i,\text{max}}^0 - G_{i,\text{min}}^0}, \tag{11}$$

using the average, maximum, and minimum symmetry function values obtained from the full reference data set. The derivatives are modified correspondingly:

$$\frac{\partial G_i}{\partial \alpha_k} = \frac{\partial G_i^0}{\partial \alpha_k} \frac{1}{G_{i,\text{max}}^0 - G_{i,\text{min}}^0}. \tag{12}$$

Parameter sets (weight parameter and bias weights) as well as average, minimum, and maximum values for each symmetry function are available online for all NNPs[14].

Comparisons of potentials with and without explicit consideration of long-range electrostatics[15,16] have shown that there is no significant difference in the accuracy of the energies and forces in the training and in the test set for the chosen cutoff radius of 6.35 Å. Consequently, long-range electrostatics were not included explicitly and the use of Ewald summation techniques is avoided, ensuring a linear scaling of the computational costs with system size.

Individual data sets for each reference method were generated in an iterative process starting with initial data sets that were systematically extended. Reference data sets were always randomly split into a training set, containing 90% of all configurations, and an independent test set, containing the remaining 10% of configurations. Initial reference configurations contain crystalline configurations obtained from DFT relaxations and liquid configurations from force field MD simulations. Configurations of eight different ice polymorphs (ice Ih, XI, IX, II, XIV, XV, VIII, and X) at different lattice constants

were included. In addition to the fully relaxed configurations, also distorted structures with randomly displaced atomic positions were used. Initial configurations for liquid water were taken from force field MD simulations at different temperatures, employing the simulation package GROMACS[17] and the flexible non-polarizable SPC/Fw[18] water model, and recomputed with the respective reference method. Simulations with 16 and 32 water molecules were performed at the experimental density of water, while unit cells containing 64 water molecules were employed for NpT simulations at various densities. Based on these data, preliminary NNPs were constructed and employed in structural relaxations and MD simulations (with units cells containing up to 128 water molecules) at various temperatures and pressures to generate new configurations, which were then recomputed by DFT and added to the initial data sets. After four cycles of refinement the NNPs were converged and applied in production runs. Final reference data sets contain about 7,000 periodic configurations per NNP, corresponding to $\approx$ 1,700,000 force components, which have also been used for training the NNPs. As illustrated in Fig. S2, the energy error does not grow with increasing binding energy, and all configurations, independent of their location in the energy vs. volume phase space, are equally well represented.

B. Viscosities and Diffusion Coefficients

Shear viscosities η were computed from the Green-Kubo relation,

$$\eta = \frac{V}{k_B T} \int_0^\infty \langle P_{\alpha\beta}(t) P_{\alpha\beta}(0) \rangle dt, \tag{13}$$

where $\langle P_{\alpha\beta}(t) P_{\alpha\beta}(0) \rangle$ is the autocorrelation function of the stress tensor element $P_{\alpha\beta}$. Autocorrelation functions (cf. Fig. S4a) were averaged over the five independent components P_{xy}, P_{xz}, P_{yz}, $\frac{1}{2}(P_{xx} - P_{yy})$, and $\frac{1}{2}(P_{yy} - P_{zz})$. A value of 3 ps was chosen for the upper limit of the integral (see Fig. S4b). As shown in Fig. S4c, the final viscosity values are essentially system size independent.

Diffusion coefficients D_{PBC} were computed from mean squared displacements,

$$D_{\text{PBC}} = \lim_{t \to \infty} \frac{1}{6} \frac{d}{dt} \langle |\mathbf{r}(t) - \mathbf{r}(0)|^2 \rangle. \tag{14}$$

In order to correct for finite size effects, we obtained system size independent diffusion coefficients D_0 (cf. Fig. S4d) from the relation[19,20],

$$D_0 = D_{\text{PBC}} + \frac{k_B T \xi}{6\pi} \frac{1}{\eta L}, \tag{15}$$

where L is the length of the cubic simulation cell and $\xi = 2.837297$. The viscosity values and diffusion coefficients shown in Fig. 1 in the main text were computed for 512 water molecules. Error bars were estimated from the

standard error of the mean of the values obtained from the 32 independent NVE trajectories. Due to the very low water mobility in the BLYP simulations, converged viscosity values could not be computed for $T = 275$ and $300\,\mathrm{K}$.

C. Hydrogen Bond Analysis

The hydrogen bond (HB) autocorrelation functions $c(t)$ and $n(t)$, shown in Fig. 1 in the main text, were obtained employing the HB criterion by Luzar and Chandler[21] (wherein a pair of water molecules is considered hydrogen bonded if $r_{OO} < 3.5\,\text{Å}$ and $\beta = \angle H_D-O_D \cdots O_A < 30°$). The autocorrelation function $c(t)$ is given by,

$$c(t) = \frac{\langle h(t)h(0) \rangle}{h}, \qquad (16)$$

where $h(t)$ is unity if a particular pair of water molecules is hydrogen bonded at time t and is zero otherwise[22]. $c(t)$ is the intermittent HB autocorrelation function which does not require that a particular HB remains continuously intact but also counts HBs that break and subsequently reform. The autocorrelation function $n(t)$ gives the time-dependent probability that a water pair that is *not* hydrogen bonded remains within a distance of $3.5\,\text{Å}$ from each other and is defined by,

$$n(t) = \frac{\langle h(0)[1 - h(t)]H(t) \rangle}{h}, \qquad (17)$$

where $H(t)$ is set to unity if the water pair is closer than $3.5\,\text{Å}$ and is zero otherwise. In addition to the correlation functions, forward and backward rate constants and HB relaxation times and lifetimes were computed based on the Luzar-Chandler model[22] and are reported in Table S3.

D. Properties of Crystalline Water

Structural and energetical properties of seven low- to high-pressure ice polymorphs (ice Ih, XI, IX, II, XIV, XV, and VIII) were computed using the NNPs and DFT and compared to the corresponding experimental values[23–28]. Experimental lattice energies (taken from Ref.[26]) are extrapolated to 0 K and do not contain zero-point contributions. Energy vs. volume curves were computed by isotropic variation[29] of the experimental lattice parameters followed by a full relaxation of all atoms in the unit cell employing the L-BFGS algorithm[30]. As shown in Fig. S5, curves obtained from NNP calculations closely reproduce the reference DFT values and the inclusion of vdW interactions leads to a significantly improved agreement with experiment. Equilibrium lattice energies and volumes were obtained by fitting the Murnaghan equation of state[31] to the energy vs. volume curves. Deviations of the equilibrium values between NNP and DFT are only a small fraction of the errors of the DFT values with respect to experiment.

E. Dielectric Properties

Molecular dipole moments $\boldsymbol{\mu}$ and dielectric constants ϵ_r were obtained by post-processing independent configurations from NNP simulations in the NVT ensemble at $T = 300\,\mathrm{K}$ employing unit cells containing 128 molecules at the experimental density ($\rho = 0.9965\,\mathrm{g/cm^3}$). After equilibrating for $1\,\mathrm{ns}$, simulations were carried out for $3\,\mathrm{ns}$ and $7\,\mathrm{ns}$ for the RPBE- and BLYP-based potentials, respectively. Due to their reduced water dynamics (cf. Fig. 1 in the main text), longer simulation times were employed for the BLYP-based NNPs. Configurations were extracted every $20\,\mathrm{ps}$ and maximally localized Wannier functions[32] (MLWFs) were computed using the projector augmented wave[33,34] (PAW)-based Vienna *ab initio* simulation package[35–38] (VASP, employing a plane-wave cutoff of 700 eV) and the WANNIER90 program[39]. Molecular dipole moments $\boldsymbol{\mu}$ were computed using the Wannier function centers (WFCs) of the four MLWFs representing the valence electrons. The dielectric constant ϵ_r was calculated using the the relation,

$$\epsilon_r = \frac{1}{3k_B\epsilon_0 TV}\left(\langle \mathbf{M}^2 \rangle - \langle \mathbf{M} \rangle^2\right) + \epsilon_\infty, \qquad (18)$$

where T is the temperature, V is the box volume, $\mathbf{M} = \sum_i^N \mu_i$ is the total dipole moment of the simulation box and ϵ_∞ is the permittivity of vacuum ($\epsilon_\infty = 1.8$[40]). Fig. S6 shows the distribution of the molecular dipole moment and the convergence of ϵ_r with simulation time for all NNPs. The average magnitudes of the molecular dipole moment and the final values for the dielectric constant are reported in Table S8.

F. Density Isobars

In order to evaluate the influence of system size on the computed density isobars, we performed additional NNP simulations at temperatures around the density maximum for a larger system ($n\,H_2O = 360$) which are compared to the results obtained for the smaller system ($n\,H_2O = 128$). As shown in Fig. S7, no significant difference between the two density isobars is visible, indicating that the results obtained for 128 molecules are converged with respect to system size.

Values for the temperature of maximum density, the density at the maximum, and the thermal expansivity, α,

$$\alpha = -\frac{1}{\rho}\left(\frac{\partial \rho}{\partial T}\right)_p, \qquad (19)$$

at ambient conditions obtained for simulations cells containing 128 molecules are reported in Table S4.

G. Melting Temperatures

Melting temperatures of ice Ih were computed employing the interface pinning method[41,42]. The method is based on stabilizing a liquid-solid interface in an elongated simulation box (see Fig. 2d in the main text) by pinning it with an order parameter-dependent bias energy $V_B(R) = \frac{\kappa}{2}\left[Q(\mathbf{R}) - a\right]^2$, where κ is a spring constant and a is the anchor point. The order parameter $Q(\mathbf{R})$ quantifies the crystalline fraction of the system. The difference $\Delta\mu$ in chemical potential between the solid and the liquid phase follows from the average deviation of the order parameter from the anchor point. The melting temperature is then determined via an iterative scheme based on the Newton-Raphson method described in Ref.[42]. The order parameter was chosen[42] as $Q(\mathbf{R}) = |\rho_{\mathbf{k}}|$ where $\mathbf{k} = (2\pi n_x/X, 2\pi n_y/Y, 0)$ and $n_x = 6, n_y = 12$. The spring constant and anchor point of the interface pinning term were set to $\kappa = 0.05\,\text{eV}$ and $a = 19.0$. All interface pinning simulations were performed using 2304 water molecules, a time step of 1 fs and a pressure of $p = 1\,\text{bar}$. The total simulation time was 15 ns. The melting temperatures and corresponding errors were derived as follows: from interface pinning simulations we extract pairs of $(T, \Delta\mu \pm \sigma_{\Delta\mu})$, where $\Delta\mu = \mu_{\text{liquid}} - \mu_{\text{solid}} = \frac{\kappa\Delta Q}{N}\left[\langle Q\rangle' - a\right]$ and $\sigma_{\Delta\mu}$ is determined from block averages. In the vicinity of T_m we assume a linear dependency $\Delta\mu(T) = kT + d$ and use the pairs $(T, \Delta\mu \pm \sigma_{\Delta\mu})$ to fit k and d. We derive T_m via $\Delta\mu(T_m) = 0$ and the errors using 68% confidence interval bands.

H. Melting Point Correction

Due to small differences between the NNP and the DFT energies, the melting temperature T_m^{NNP} obtained with the NNP may differ from the melting temperature T_m^{DFT} of the reference method. Using thermodynamic perturbation theory, we next derive a correction term,

$$\Delta T_m = T_m^{\text{DFT}} - T_m^{\text{NNP}}, \tag{20}$$

which accounts for this difference.

We first approximate the DFT Gibbs free energy of the liquid phase $G_l^{\text{DFT}}(p,T)$ and the solid phase $G_s^{\text{DFT}}(p,T)$ by a Taylor expansion at $T = T_m^{\text{NNP}}$, truncated after the linear term (see Fig. S8a, p omitted for clarity),

$$G_l^{\text{DFT}}(T) \approx G_l^{\text{DFT}}(T_m^{\text{NNP}}) + \left.\frac{\partial G_l^{\text{DFT}}}{\partial T}\right|_{T_m^{\text{NNP}}} (T - T_m^{\text{NNP}}),$$

$$G_s^{\text{DFT}}(T) \approx G_s^{\text{DFT}}(T_m^{\text{NNP}}) + \left.\frac{\partial G_s^{\text{DFT}}}{\partial T}\right|_{T_m^{\text{NNP}}} (T - T_m^{\text{NNP}}).$$

Using the equivalence $G_l^{\text{DFT}} = G_s^{\text{DFT}}$ at $T = T_m^{\text{DFT}}$ and the relation $\frac{\partial G}{\partial T} = -S$ we obtain,

$$\Delta T_m = \frac{G_l^{\text{DFT}}(T_m^{\text{NNP}}) - G_s^{\text{DFT}}(T_m^{\text{NNP}})}{S_l^{\text{DFT}}(T_m^{\text{NNP}}) - S_s^{\text{DFT}}(T_m^{\text{NNP}})}. \tag{21}$$

By expressing G^{DFT} and S^{DFT} in terms of G^{NNP} and S^{NNP}, respectively, and inserting in Eq. (21) we arrive at the final equation for ΔT_m,

$$\Delta T_m = \frac{\Delta G_l - \Delta G_s}{S_l^{\text{NNP}} - S_s^{\text{NNP}} + \Delta S_l - \Delta S_s}, \tag{22}$$

where $\Delta G = G^{\text{DFT}} - G^{\text{NNP}}$ and $\Delta S = S^{\text{DFT}} - S^{\text{NNP}}$. All quantities of Eq. (22) are evaluated at $T = T_m^{\text{NNP}}$. The difference $S_l^{\text{NNP}} - S_s^{\text{NNP}}$ is the entropy of fusion and is known from the interface pinning simulations (see Table S5). With

$$\Delta G = \langle E\rangle_{\text{DFT}} - \langle E\rangle_{\text{NNP}} - T\Big(\langle S\rangle_{\text{DFT}} - \langle S\rangle_{\text{NNP}}\Big)$$
$$+ p\Big(\langle V\rangle_{\text{DFT}} - \langle V\rangle_{\text{NNP}}\Big) = \Delta\overline{E} - T\Delta\overline{S} + p\Delta\overline{V} \tag{23}$$

we can find an expression for ΔS,

$$\Delta S = \frac{1}{T}\Big(\Delta\overline{E} + p\Delta\overline{V} - \Delta G\Big). \tag{24}$$

Here $\langle\ldots\rangle_{\text{NNP}}$ and $\langle\ldots\rangle_{\text{DFT}}$ refer to averages corresponding to the NNP and the DFT potential-energy surface, respectively. Using thermodynamic perturbation theory, the averages $\Delta\overline{E}$, $\Delta\overline{V}$, and ΔG can be expressed as,

$$\Delta\overline{E} = \frac{\langle e^{-\beta\Delta E}E^{\text{DFT}}\rangle_{\text{NNP}}}{\langle e^{-\beta\Delta E}\rangle_{\text{NNP}}} - \langle E\rangle_{\text{NNP}}, \tag{25}$$

$$\Delta\overline{V} = \frac{\langle e^{-\beta\Delta E}V^{\text{DFT}}\rangle_{\text{NNP}}}{\langle e^{-\beta\Delta E}\rangle_{\text{NNP}}} - \langle V\rangle_{\text{NNP}},$$

$$\Delta G = -k_{\text{B}}T\ln\langle e^{-\beta\Delta E}\rangle_{\text{NNP}},$$

where $\Delta E = E^{\text{DFT}} - E^{\text{NNP}}$ and $\beta = 1/k_{\text{B}}T$. The quantities needed to compute ΔT_m are obtained in the following way:

- NNP simulations for the solid and the liquid phase are performed in the NpT ensemble at $T = T_m^{\text{NNP}}$ and $p = 1\,\text{bar}$.

- Independent configurations are extracted from the trajectories and their energies are recomputed with the corresponding DFT method in order to obtain E^{DFT}.

- The averages $\langle e^{-\beta\Delta E}\rangle_{\text{NNP}}$, $\langle e^{-\beta\Delta E}E^{\text{DFT}}\rangle_{\text{NNP}}$, $\langle e^{-\beta\Delta E}V^{\text{DFT}}\rangle_{\text{NNP}}$, $\langle E\rangle_{\text{NNP}}$, and $\langle V\rangle_{\text{NNP}}$ are computed both for the solid and the liquid phase.

- ΔG_l, ΔG_s, ΔS_l, and ΔS_s are determined from Eqs. (25) and (24).

- ΔT_m is computed using Eq. (22).

NpT simulation for all NNPs were performed using 128 molecules for both phases and total simulation times of 14 ns per NNP. After discarding 4 ns for the purpose of equilibration, configurations were extracted every 20 ps and their energies were recomputed with the corresponding reference DFT method. Fig. S8b-d shows the convergence of ΔG, ΔS, and ΔT_m with the number of configurations used to obtain the averages given in Eq. (25). The final values for T_m^{DFT}, T_m^{NNP}, and ΔT_m are reported in Table S5. For all NNPs the correction term is positive, which originates from a positive shift of the NNP energies of the solid phase with respect to the DFT values (see Fig. S8e-h).

I. Neighbor Distribution

The structure of water was analyzed by decomposing the oxygen-oxygen radial distribution function into contributions from neighboring molecules (similar to the analysis in Ref.[43]) using the analysis tool TRAVIS[44]. In order to visualize the location of first-shell and second-shell molecules, the centroid of the corresponding distribution functions $P_{1^{\mathrm{st}}-4^{\mathrm{th}}}(r_{\mathrm{OO}})$ and $P_{5^{\mathrm{th}}-8^{\mathrm{th}}}(r_{\mathrm{OO}})$ was computed, and the position of the centroid,

$$C_x = \frac{\int P(r_{\mathrm{OO}}) r_{\mathrm{OO}}\, dr_{\mathrm{OO}}}{\int P(r_{\mathrm{OO}})\, dr_{\mathrm{OO}}}, \qquad (26)$$

was plotted against temperature. Error bars for C_x were estimated by averaging over values obtained from non-overlapping time intervals of a length of 0.5 ns.

J. Hydrogen Bond Fluctuation

HB strengths were measured in terms of fluctuations in the distribution $P(\beta)$ of the HB angle $\beta = \angle H_D - O_D \cdots O_A$. Cone corrected[45] probability density functions $P(\beta)$ were obtained by computing β between a reference molecule and its four nearest neighbors. Fluctuations were obtained from the half width at half maximum (HWHM) of a Gaussian fit to the probability density function. Error bars for HWHM $P(\beta)$ were estimated by averaging over values obtained from non-overlapping time intervals of a length of 0.5 ns. Angular probability density functions $P(\beta)$ and combined angular/radial probability density functions were

II. SI FIGURES

computed using TRAVIS[44]. Molecular dynamics simulations using six empirical water models (TIP3P[46], SPC/E[47], TIP4P[46], TIP4P-Ew[48], TIP4P/2005[49], and TIP4P/Ice[50]) at regions close to their melting temperature[51] were carried out to confirm the correlation between hydrogen bond strength and melting temperature. These simulations were performed using 2880 water molecules with a time step of $\Delta t = 2$ fs. At each temperature, a trajectory of 5 ns length was generated to extract hydrogen bond information. The fluctuations of the hydrogen bond angle for the empirical water models are depicted in Fig. S9.

K. van der Waals Interactions

We employed the DFT-D3 method[11] in order to account for vdW interactions. In this approach the two-body van der Waals interaction $E_{\mathrm{vdW}}^{(2)}$ for atom pairs AB at distance r_{AB} is computed from 6th- and 8th-order dispersion coefficients $C_{6/8}^{AB}$ that depend on their chemical environment (by being a function of fractional coordination numbers CN, cf. Ref.[11]),

$$E_{\mathrm{vdW}}^{(2)} = -\sum_{A<B}^{N_{\mathrm{pairs}}} \left(\frac{C_6^{AB}(CN)}{r_{AB}^6} f_{d,6}(r_{AB}) \right. \qquad (27)$$
$$\left. + s_8 \frac{C_8^{AB}(CN)}{r_{AB}^8} f_{d,8}(r_{AB}) \right).$$

The range of the vdW correction is determined by damping functions $f_{d,n}$, which screen the vdW contribution to zero at short distances (zero-damping) in order to avoid near singularities,

$$f_{d,n}(r_{AB}) = \left(1 + 6 \left(\frac{r_{AB}}{s_{r,n} R_0^{AB}} \right)^{-\alpha_n} \right)^{-1}. \qquad (28)$$

The parameters s_8 and $s_{r,6}$ are the only two density-functional dependent parameters of the D3 method (cf. Table S6). Van der Waals pair interactions, $E_{\mathrm{vdW(OH/OO)}}$, for oxygen-hydrogen and oxygen-oxygen pairs (shown in Fig. 5 of the main text and in Fig. S10, respectively), and average values of $C_{6/8}^{AB}$ coefficients reported in Table S6 were computed by employing a modified version of the dftd3 program[52].

As shown in Table S6, for both density-functionals the $C_{6/8}^{AB}$ coefficients are essentially identical, responsible for the different range of the vdW pair interaction are solely the $s_{r,6}$ and s_8 parameters.
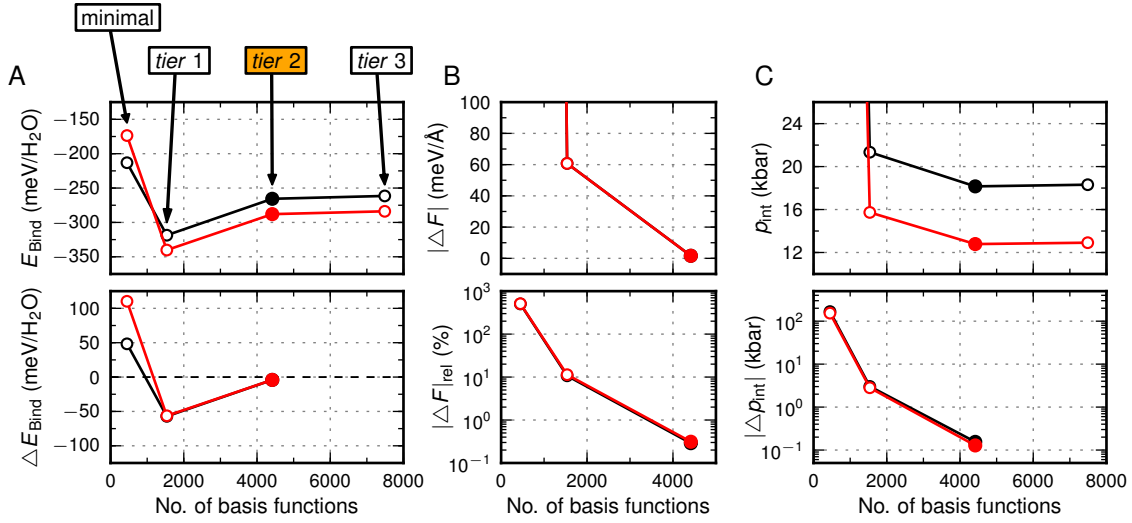
Figure S1. **Basis set convergence.** Convergence of binding energies, E_{Bind} (A), forces, F (B), and instantaneous pressure, p_{int} (C) with basis set size for two typical liquid water configurations containing 64 water molecules. $\Delta E_{\text{Bind}} = E_{\text{Bind}} - E_{\text{Bind}, \, tier\, 3}$, $|\Delta F| = \frac{1}{3N_{\text{atoms}}} \sum_{i=1}^{3N_{\text{atoms}}} |F_i - F_{i, \, tier\, 3}|$, $|\Delta F|_{\text{rel}} = 100 \times |\Delta F| / \frac{1}{3N_{\text{atoms}}} \sum_{i=1}^{3N_{\text{atoms}}} |F_{i, \, tier\, 3}|$, $p_{\text{int}} = -\frac{1}{3} tr(\text{stress tensor})$, and $|\Delta p_{\text{int}}| = |p_{\text{int}} - p_{\text{int}, \, tier\, 3}|$. The $tier$ 2 basis was chosen as production basis set for all reference calculations used to train the NNPs.
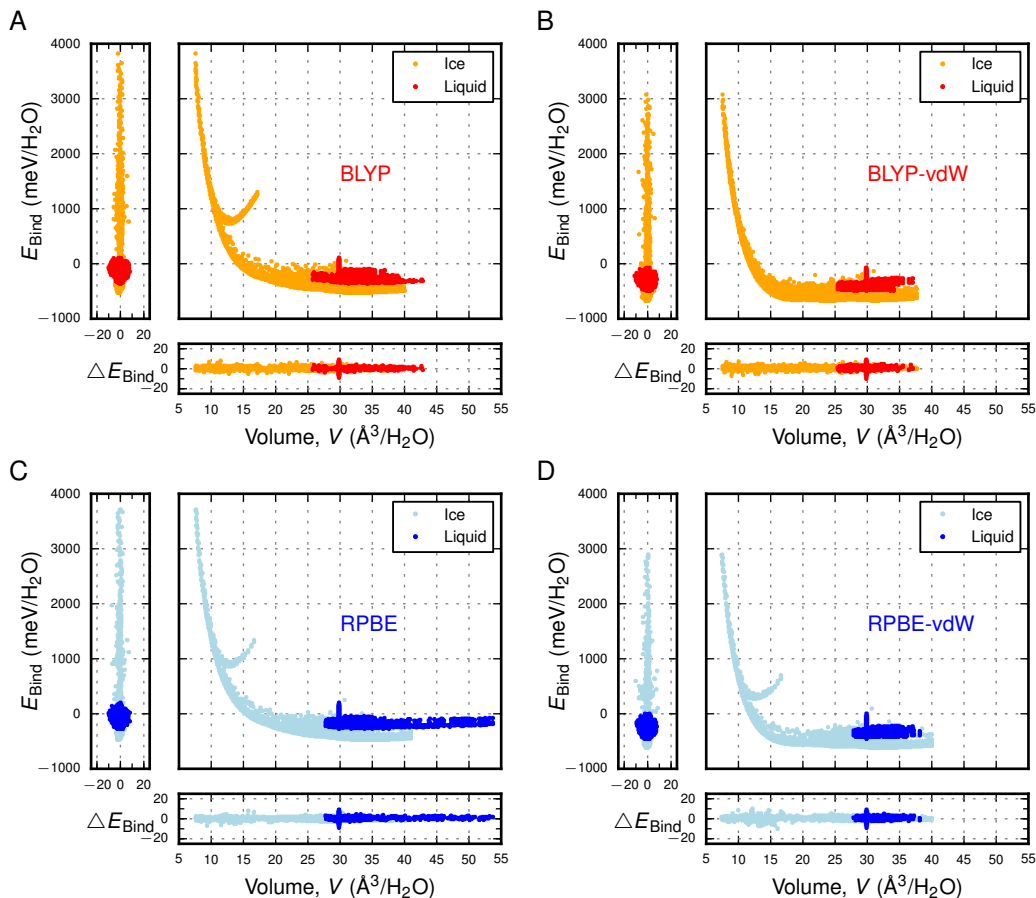
Figure S2. **Accuracy and distribution of reference configurations.** Energy error $\Delta E_{\text{Bind}} = E_{\text{Bind, NNP}} - E_{\text{Bind, DFT}}$ (in meV/H_2O) as function of binding energy and volume, and location of reference configurations in the E_{Bind} vs. V space for NNPs based on BLYP (A), BLYP-vdW (B), RPBE (C), and RPBE-vdW (D).
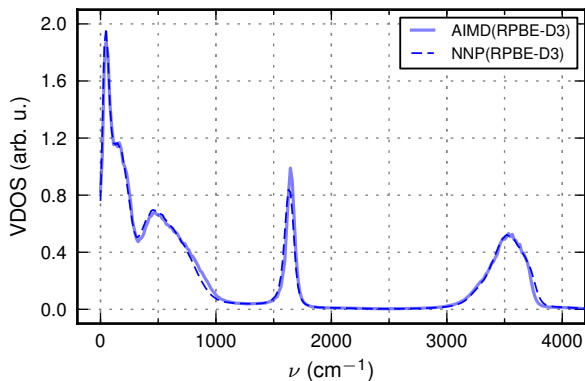

Figure S3. **VDOS spectrum.** Vibrational density of state (VDOS) computed from velocity autocorrelation functions obtained from RPBE-D3-based NNP simulations at $T = 300\,\text{K}$ and $\rho = 1\,\text{g/cm}^3$ compared to results from *ab initio* simulations[53].
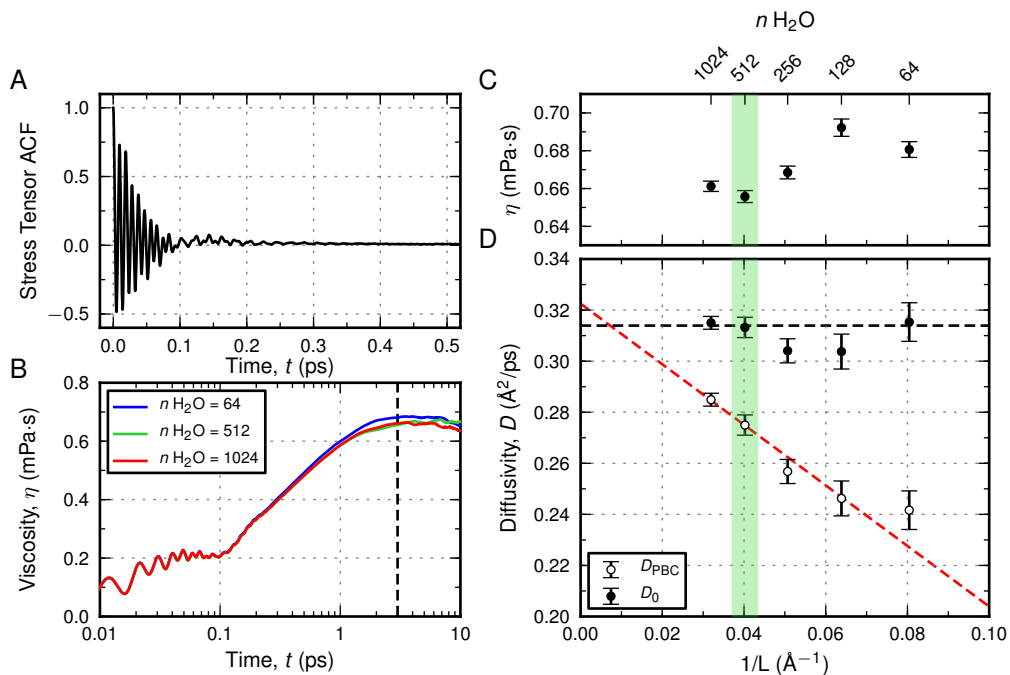
Figure S4. **System-size dependence of diffusion coefficient and viscosity.** (A) Normalized stress autocorrelation function for a system of 64 water molecules. (B) Running values of the viscosity η for different system sizes computed from the stress autocorrelation function using the Green-Kubo formula. The dashed line indicates the upper limit used for computing the final viscosity values. (C-D) Viscosity, and uncorrected D_{PBC} and corrected D_0 diffusion coefficients as function of inverse box length $1/L$. The red and black dashed lines are weighted least squares fits of the uncorrected and corrected diffusion coefficients, respectively. All values reported here are obtained from NNP simulations based on the vdW-corrected RPBE density-functional performed at $T = 300\,\text{K}$ and $\rho = 1\,\text{g/cm}^3$. The green bar indicates the system size used for computing the results reported in Fig. 1 of the main text.
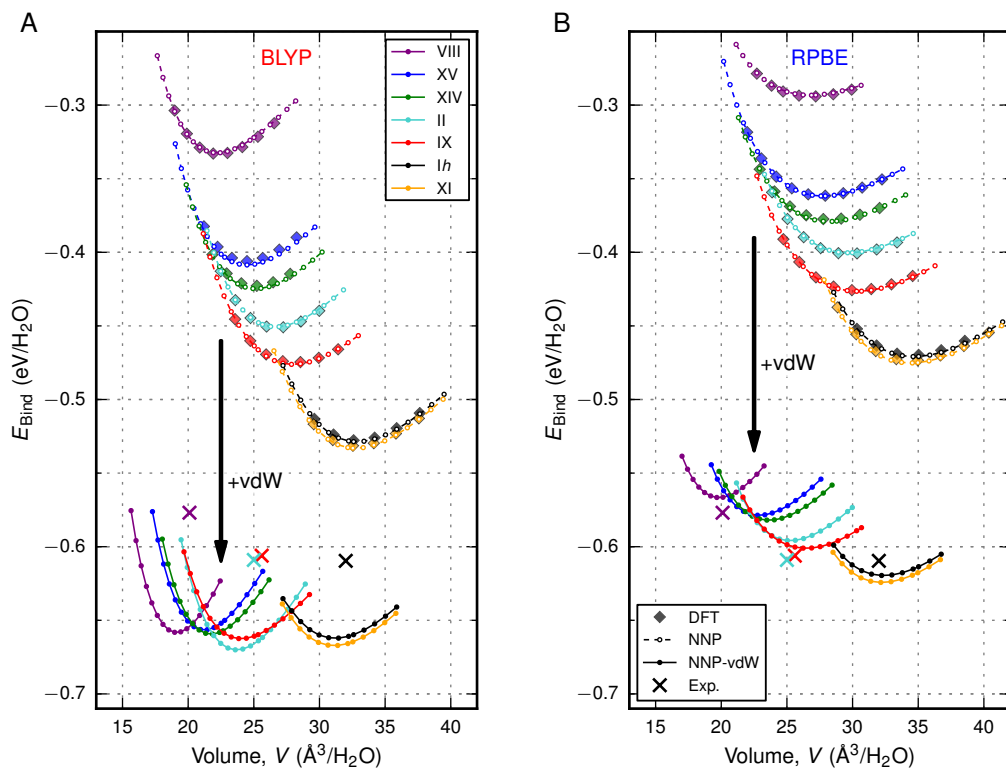
Figure S5. **Energy vs. volume curves.** Lattice energy ($T = 0\,\mathrm{K}$) as function of volume of seven ice phases computed with DFT and NNPs based on BLYP / BLYP-vdW (A) and RPBE / RPBE-vdW (B). For ice Ih, IX, II, and VIII also the experimental equilibrium values[23,25,26] are shown.
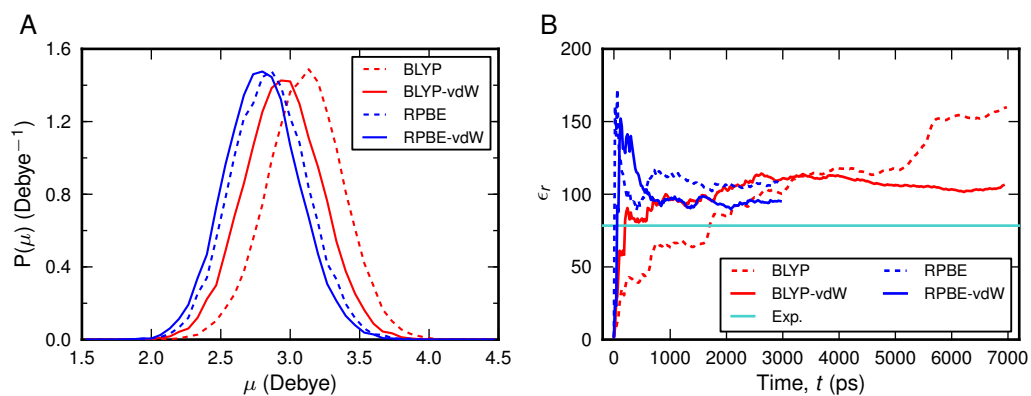
Figure S6. **Dielectric properties.** (A) Probability density function P(μ) of the molecular dipole moment magnitude μ computed from maximally localized Wannier functions evaluated at configurations sampled by NNPs at $300\,\mathrm{K}$. (B) Convergence of the cumulative average of the dielectric constant ϵ_r as function of simulation time.
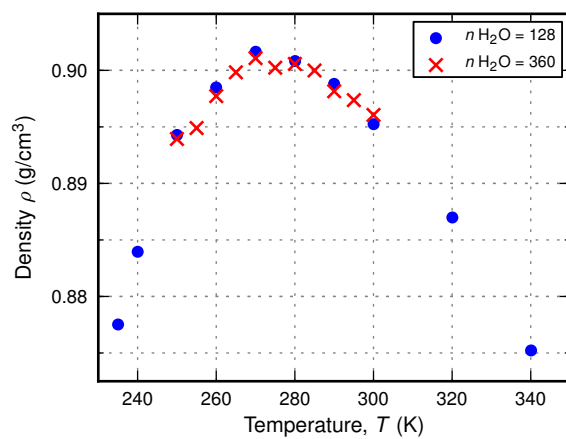
Figure S7. **System size dependence of the density isobar.** Density isobars at $p = 1$ bar obtained from NNP(RPBE-vdW) simulations employing simulation cells containing 128 (blue filled circles) and 360 (red crosses) water molecules, respectively.
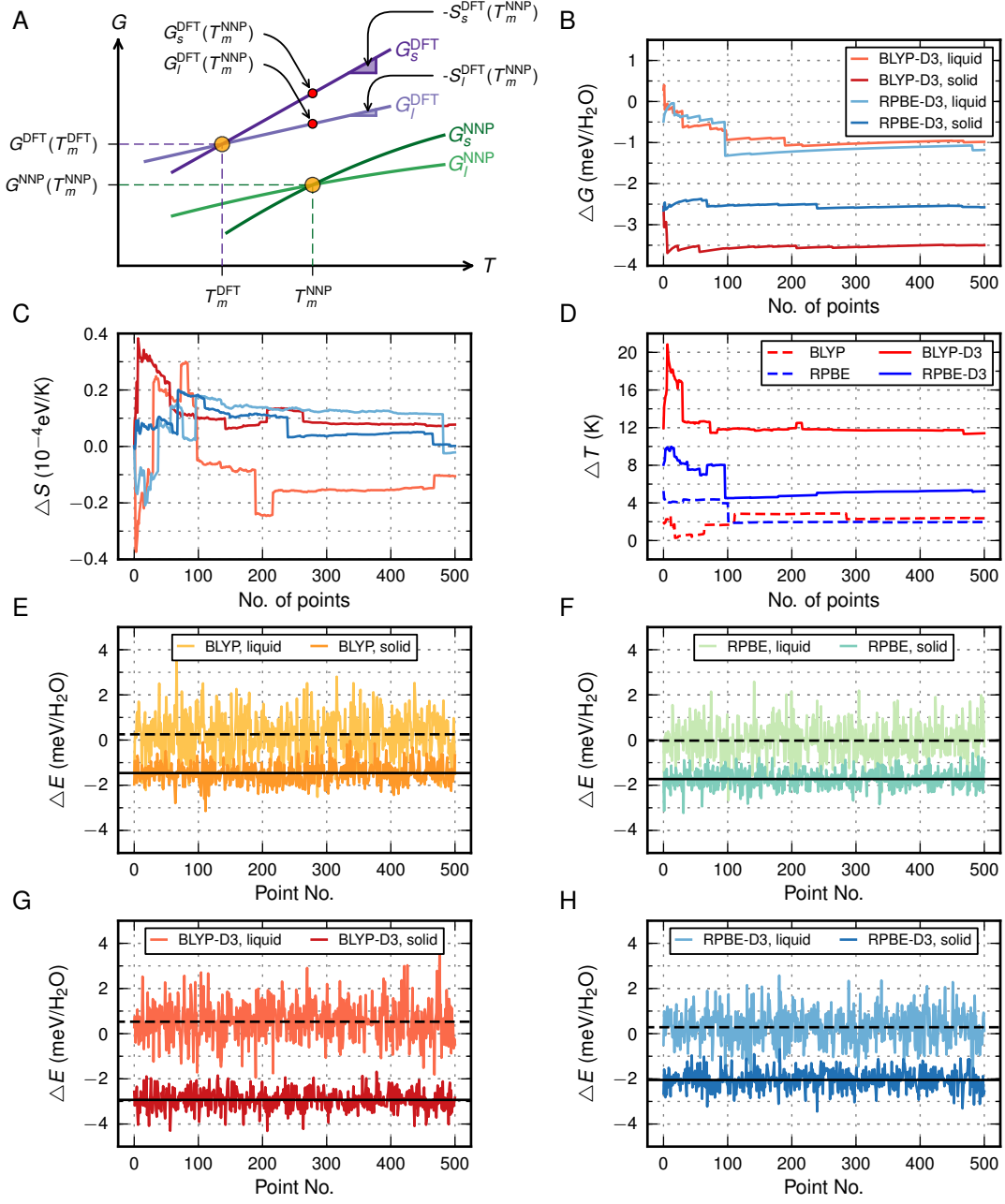
Figure S8. **Melting Point Correction.** (A) The correction term $\Delta T_m = T_m^{\mathrm{DFT}} - T_m^{\mathrm{NNP}}$ is estimated by expanding the DFT Gibbs free energy G^{DFT} as a Taylor series around $T = T_m^{\mathrm{NNP}}$. The slope of the linear expansion is given by the negative entropy of fusion $-S^{\mathrm{DFT}}$. (B-C) Convergence of free energy difference $\Delta G = G^{\mathrm{DFT}} - G^{\mathrm{NNP}}$ and entropy difference $\Delta S = S^{\mathrm{DFT}} - S^{\mathrm{NNP}}$ as function of the number of configurations used to obtain the average quantifies given in Eq. (25) for the vdW-corrected NNPs. (D) Convergence of the melting point correction term ΔT for all NNPs. (E-H) Energy difference $\Delta E = E^{\mathrm{DFT}} - E^{\mathrm{NNP}}$ for all configurations used for the melting point correction. The black solid and black dashed lines indicate the average energy difference for the solid and the liquid phase, respectively.
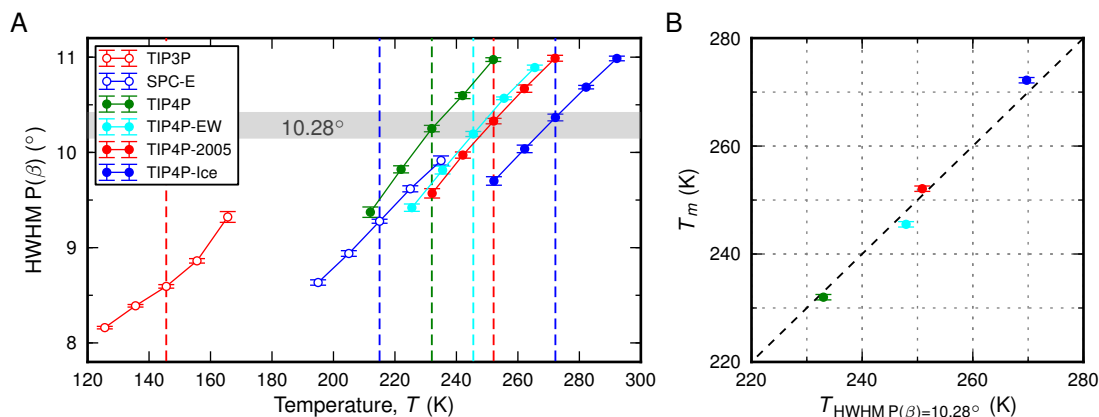
Figure S9. **Hydrogen bond strength and melting temperature for common empirical water models.** (A) Fluctuation in the hydrogen bond angle β close to the melting temperature of ice Ih[51], obtained from simulations using the six empirical water models[46–50] given in the legend box. Dashed vertical lines denote the melting temperature of the respective water model. (B) Correlation between melting temperature T_m and temperature of a hydrogen bond fluctuation of $10.28°$ computed for water models based on four-site interaction potentials (TIP4P-x).
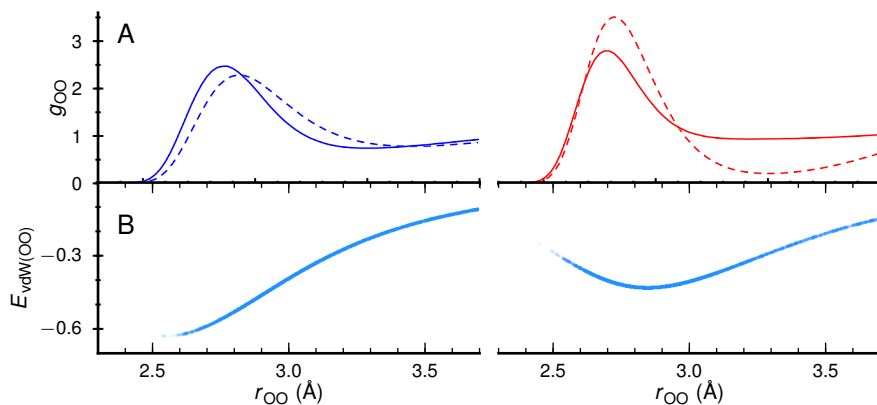
Figure S10. **Effect of van der Waals interactions on oxygen-oxygen distributions.** (A) Oxygen-oxygen radial distribution functions g_{OO} from NNP simulations at $300\,K$ based on the RPBE (left) and BLYP (right) density-functionals with (solid lines) and without (dashed lines) vdW corrections. (B) Van der Waals pair interaction energy $E_{vdW(OO)}$ (in k_BT) between pairs of oxygen atoms as a functions of the pair distance r_{OO} obtained from the NNP simulations.

III. SI TABLES

Table S1. Symmetry function parameters for hydrogen.

No.	Element j	Element k	r_s	η	λ	ζ
1	H	—	0.0	0.001	—	—
2	O	—	0.0	0.001	—	—
3	H	—	0.0	0.010	—	—
4	O	—	0.0	0.010	—	—
5	H	—	0.0	0.030	—	—
6	O	—	0.0	0.030	—	—
7	H	—	0.0	0.060	—	—
8	O	—	0.0	0.060	—	—
9	O	—	0.9	0.150	—	—
10	H	—	1.9	0.150	—	—
11	O	—	0.9	0.300	—	—
12	H	—	1.9	0.300	—	—
13	O	—	0.9	0.600	—	—
14	H	—	1.9	0.600	—	—
15	O	—	0.9	1.500	—	—
16	H	—	1.9	1.500	—	—
17	O	O	0.0	0.001	-1.0	4.0
18	O	O	0.0	0.001	1.0	4.0
19	H	O	0.0	0.010	-1.0	4.0
20	H	O	0.0	0.010	1.0	4.0
21	H	O	0.0	0.030	-1.0	1.0
22	O	O	0.0	0.030	-1.0	1.0
23	H	O	0.0	0.030	1.0	1.0
24	O	O	0.0	0.030	1.0	1.0
25	H	O	0.0	0.070	-1.0	1.0
26	H	O	0.0	0.070	1.0	1.0
27	H	O	0.0	0.200	1.0	1.0 [a]

[a] Parameters r_s (in Bohr), η (in Bohr^{-2}), λ, and ζ of atom-centered symmetry functions of type G^2 (radial, nos. $1-16$) and type G^4 (angular, nos. $17-27$) used to describe the local chemical environments of hydrogen atoms. The cutoff radius r_c is 12 Bohr (≈ 6.35 Å) for all symmetry functions.

Table S2. Symmetry function parameters for oxygen.

No.	Element j	Element k	r_s	η	λ	ζ
1	H	—	0.0	0.001	—	—
2	O	—	0.0	0.001	—	—
3	H	—	0.0	0.010	—	—
4	O	—	0.0	0.010	—	—
5	H	—	0.0	0.030	—	—
6	O	—	0.0	0.030	—	—
7	H	—	0.0	0.060	—	—
8	O	—	0.0	0.060	—	—
9	H	—	0.9	0.150	—	—
10	O	—	4.0	0.150	—	—
11	H	—	0.9	0.300	—	—
12	O	—	4.0	0.300	—	—
13	H	—	0.9	0.600	—	—
14	O	—	4.0	0.600	—	—
15	H	—	0.9	1.500	—	—
16	O	—	4.0	1.500	—	—
17	H	O	0.0	0.001	-1.0	4.0
18	O	O	0.0	0.001	-1.0	4.0
19	H	O	0.0	0.001	1.0	4.0
20	O	O	0.0	0.001	1.0	4.0
21	H	H	0.0	0.010	-1.0	4.0
22	H	H	0.0	0.010	1.0	4.0
23	H	H	0.0	0.030	-1.0	1.0
24	H	O	0.0	0.030	-1.0	1.0
25	O	O	0.0	0.030	-1.0	1.0
26	H	H	0.0	0.030	1.0	1.0
27	H	O	0.0	0.030	1.0	1.0
28	O	O	0.0	0.030	1.0	1.0
29	H	H	0.0	0.070	-1.0	1.0
30	H	H	0.0	0.070	1.0	1.0 [a]

[a] Parameters r_s (in Bohr), η (in Bohr^{-2}), λ, and ζ of atom-centered symmetry functions of type G^2 (radial, nos. 1 – 16) and type G^4 (angular, nos. 17 – 30) used to describe the local chemical environments of oxygen atoms. The cutoff radius r_c is 12 Bohr (≈ 6.35 Å) for all symmetry functions.

Table S3. Hydrogen bond kinetics.

Model	τ_{rlx} (ps)	k (ps^{-1})	k' (ps^{-1})	τ_{HB} (ps)	$\tau_{\mathrm{rlx}}/\tau_{\mathrm{HB}}$	n HB
NNP(BLYP)	—	—	—	—	—	3.81
NNP(BLYP-vdW)	7.12	0.24	0.57	4.22	1.69	3.64
NNP(RPBE)	2.00	1.15	8.37	0.87	2.30	2.61
NNP(RPBE-vdW)	4.33	0.45	1.65	2.24	1.93	3.47
TIP4P	3.32	0.45	1.02	2.22	1.49	3.54 [a]

[a] Comparison of hydrogen bond relaxation time (τ_{rlx}), forward and backward rate constants (k and k'), and lifetime (τ_{HB}) based on the Luzar-Chandler model[22]. In addition, the average number of hydrogen bonds (n HB) is shown. The NNP values were obtained from simulations at $T = 300$ K. The TIP4P results were taken from Ref.[54].

Table S4. Density maximum and thermal expansivity.

Model	TMD (K)	ρ_{TMD} (g/cm^3)	$\alpha_{25\,^\circ\mathrm{C}}$ (10^{-6}/K)
NNP(BLYP)	—	—	991
NNP(BLYP-vdW)	256	1.054	435
NNP(RPBE)	—	—	2369
NNP(RPBE-vdW)	274	0.901	370
Exp.	277.13	0.99997	257.12[a]

[a] Comparison of temperature of maximum density (TMD), density at $T = $ TMD (ρ_{TMD}), and coefficient of thermal expansion at $T = 25\,^\circ$C ($\alpha_{25\,^\circ\mathrm{C}}$) obtained from NpT simulations of 128 H_2O using different NNPs. Experimental values were taken from Ref.[55].

Table S5. Density of the liquid and the solid phase and entropy of fusion.

Model	ρ_l	ρ_s	$\Delta\rho$	ΔS
BLYP	0.752	0.840	-0.088	2.48
BLYP-vdW	1.053	0.915	0.138	2.39
RPBE	0.678	0.786	-0.108	3.34
RPBE-vdW	0.904	0.864	0.040	2.69
Exp.	0.99984	0.91670	0.08314	2.28[a]

[a] Density values of the liquid (ρ_l) and the solid ice Ih phase (ρ_s) together with the density difference ($\Delta\rho = \rho_l - \rho_s$) (in g/cm^3) and entropy of fusion ΔS (in 10^{-4}eV/K) obtained from interface pinning simulations using different NNPs. Experimental values were taken from[56].

Table S6. Corrected melting temperatures.

	T_m^{DFT}(K)	T_m^{NNP}(K)	ΔT_m(K)
NNP(BLYP)	323 ± 3	321 ± 3	2.4
NNP(BLYP-vdW)	283 ± 2	272 ± 2	11.4
NNP(RPBE)	267 ± 2	265 ± 2	2.0
NNP(RPBE-vdW)	274 ± 3	269 ± 3	5.2 [a]

[a] Corrected melting temperatures T_m^{DFT}(K), melting temperatures obtained from interface pinning simulations T_m^{NNP}(K), and correction term ΔT_m(K) obtained from thermodynamic perturbation theory calculations.

Table S7. Van der Waals coefficients and density-functional dependent parameters.

	BLYP	RPBE
C_6^{OH}	5.436 (0.004)	5.437 (0.003)
C_8^{OH}	84.897 (0.062)	84.922 (0.042)
C_6^{OO}	10.410 (0.003)	10.413 (0.002)
C_8^{OO}	210.087 (0.067)	210.134 (0.046)
C_6^{HH}	3.092 (0.003)	3.093 (0.002)
C_8^{HH}	37.382 (0.038)	37.395 (0.026)
$s_{r,6}$	1.094	0.872
s_8	0.722	0.514[a]

[a] Environment-dependent van der Waals coefficients for oxygen-hydrogen, oxygen-oxygen, and hydrogen-hydrogen pairs, $C_{6/8}^{AB}$ (in a.u.), averaged over trajectories from NpT simulations at 300 K based on BLYP and RPBE, respectively (standard deviation is given in parentheses) and values for the two density-functional dependent parameters of the D3 method ($s_{r,6}$ and s_8).

Table S8. Dielectric properties.

Model	ϵ_r	μ (D)
NNP(BLYP)	159.8	3.11
NNP(BLYP-vdW)	106.2	2.95
NNP(RPBE)	108.9	2.85
NNP(RPBE-vdW)	95.2	2.80 [a]

[a] Dielectric constant ϵ_r and average magnitude of the molecular dipole moment μ from NNP simulations at 300 K.

REFERENCES

[1] Behler J, Parrinello M (2007) Generalized Neural-Network Representation of High-Dimensional Potential-Energy Surfaces. *Phys. Rev. Lett.* 98:146401.

[2] Behler J (2011) Atom-Centered Symmetry Functions for Constructing High-Dimensional Neural Network Potentials. *J. Chem. Phys.* 134:074106.

[3] Behler J (2014) Representing Potential Energy Surfaces by High-Dimensional Neural Network Potentials. *J. Phys.: Condens. Matter* 26:183001.

[4] Morawietz T, Behler J (2013) A Density-Functional Theory Based Neural Network Potential for Water Clusters Including van der Waals Corrections. *J. Phys. Chem. A* 117:7356.

[5] Artrith N, Kolpak AM (2014) Understanding the Composition and Activity of Electrocatalytic Nanoalloys in Aqueous Solvents: A Combination of DFT and Accurate Neural Network Potentials. *Nano Lett.* 14:2670–2676.

[6] Hammer B, Hansen LB, Norskov JK (1999) Improved Adsorption Energetics Within Density-Functional Theory Using Revised Perdew-Burke-Ernzerhof Functionals. *Phys. Rev. B* 59:7413–7421.

[7] Becke AD (1988) Density-Functional Exchange-Energy Approximation With Correct Asymptotic-Behavior. *Phys. Rev. A* 38:3098–3100.

[8] Lee CT, Yang WT, Parr RG (1988) Development of the Colle-Salvetti Correlation-Energy Formula Into a Functional of the Electron-Density. *Phys. Rev. B* 37:785–789.

[9] Blum V et al. (2009) Ab Initio Molecular Simulations with Numeric Atom-Centered Orbitals. *Comput. Phys. Commun.* 180:2175–2196.

[10] Ma ZH, Zhang YL, Tuckerman ME (2012) Ab Initio Molecular Dynamics Study of Water at Constant Pressure Using Converged Basis Sets and Empirical Dispersion Corrections. *J. Chem. Phys.* 137:044506.

[11] Grimme S, Antony J, Ehrlich S, Krieg H (2010) A Consistent and Accurate Ab Initio Parametrization of Density Functional Dispersion Correction (DFT-D) for the 94 Elements H-Pu. *J. Chem. Phys.* 132:154104.

[12] Jonchiere R, Seitsonen AP, Ferlat G, Saitta AM, Vuilleumier R (2011) Van der Waals Effects in Ab Initio Water at Ambient and Supercritical Conditions. *J. Chem. Phys.* 135:154503.

[13] Behler J (2015) RuNNer - A Neural Network Code for High-Dimensional Potential-Energy Surfaces (Lehrstuhl für Theoretische Chemie, Ruhr-Universität Bochum).

[14] Morawietz T, Singraber A, Dellago C, Behler J (2015) How van der Waals interactions determine the unique properties of water. **fig**share. http://dx.doi.org/10.6084/m9.figshare.1497907.

[15] Artrith N, Morawietz T, Behler J (2011) High-Dimensional Neural-Network Potentials for Multicomponent Systems: Applications to Zinc Oxide. *Phys. Rev. B* 83:153101.

[16] Morawietz T, Sharma V, Behler J (2012) A Neural Network Potential-Energy Surface for the Water Dimer Based on Environment-Dependent Atomic Energies and Charges. *J. Chem. Phys.* 136:064103.

[17] Van der Spoel D et al. (2005) GROMACS: Fast, Flexible, and Free. *J. Comput. Phys.* 26:1701–1718.

[18] Wu YJ, Tepper HL, Voth GA (2006) Flexible Simple Point-Charge Water Model with Improved Liquid-State Properties. *J. Chem. Phys.* 124:024503.

[19] Dünweg B, Kremer K (1993) Molecular-dynamics Simulation of A Polymer-chain In Solution. *J. Chem. Phys.* 99:6983–6997.

[20] Yeh IC, Hummer G (2004) System-Size Dependence of Diffusion Coefficients and Viscosities from Molecular Dynamics Simulations with Periodic Boundary Conditions. *J. Phys. Chem. B* 108:15873–15879.

[21] Luzar A, Chandler D (1996) Effect of Environment on Hydrogen Bond Dynamics in Liquid Water. *Phys. Rev. Lett.* 76:928–931.

[22] Luzar A, Chandler D (1996) Hydrogen-Bond Kinetics in Liquid Water. *Nature* 379:55–57.

[23] Röttger K, Endriss A, Ihringer J, Doyle S, Khus WF (1994) Lattice Constants and Thermal Expansion of H2O and D2O Ice Ih Between 10 and 265 K. *Acta Crystallogr. Sect. B-Struct. Sci.* 50:644–648.

[24] Line CMB, Whitworth RW (1996) A High Resolution Neutron Powder Diffraction Study of D2O Ice XI. *J. Chem. Phys.* 104:10008–10013.

[25] Londono JD, Kuhs WF, Finney JL (1993) Neutron Diffraction Studies of Ices III and IX on Under-Pressure and Recovered Samples. *J. Chem. Phys.* 98(6):4878–4888.

[26] Whalley E (1984) Energies of the Phases of Ice at Zero Temperature and Pressure. *J. Chem. Phys.* 81:4087–4092.

[27] Salzmann CG, Radaelli PG, Hallbrucker A, Mayer E, Finney JL (2006) The Preparation and Structures of Hydrogen Ordered Phases of Ice. *Science* 311:1758–1761.

[28] Salzmann CG, Radaelli PG, Mayer E, Finney JL (2009) Ice XV: A New Thermodynamically Stable Phase of Ice. *Phys. Rev. Lett.* 103(10):105701.

[29] Santra B et al. (2013) On the Accuracy of van der Waals Inclusive Density-functional Theory Exchange-correlation Functionals for Ice at Ambient and High Pressures. *J. Chem. Phys.* 139:154702.

[30] Liu DC, Nocedal J (1989) On the Limited Memory BFGS Method for Large-Scale Optimization. *Math. Program.* 45:503–528.

[31] Murnaghan FD (1944) The Compressibility of Media under Extreme Pressures. *Proc. Natl. Acad. Sci. U.S.A.* 30:244–7.

[32] Marzari N, Vanderbilt D (1997) Maximally localized generalized Wannier functions for composite energy bands. *Phys. Rev. B* 56:12847–12865.

[33] Blöchl PE (1994) Projector Augmented-wave Method. *Phys. Rev. B* 50:17953–17979.

[34] Kresse G, Joubert D (1999) From ultrasoft pseudopotentials to the projector augmented-wave method. *Phys. Rev. B* 59:1758–1775.

[35] Kresse G, Hafner J (1993) Ab initio molecular dynamics for liquid metals. *Phys. Rev. B* 47:558–561.

[36] Kresse G, Hafner J (1994) Ab initio molecular-dynamics simulation of the liquid-metal-amorphous-semiconductor transition in germanium. *Phys. Rev. B* 49:14251–14269.

[37] Kresse G, Furthmüller J (1996) Efficiency of ab-initio total energy calculations for metals and semiconductors using a plane-wave basis set. *Comput. Mater. Sci.* 6:15–50.

[38] Kresse G, Furthmüller J (1996) Efficient iterative schemes for ab initio total-energy calculations using a plane-wave basis set. *Phys. Rev. B* 54:11169–11186.

[39] Mostofi AA et al. (2008) wannier90: A tool for obtaining maximally-localised Wannier functions. *Comput. Phys. Commun.* 178:685–699.

[40] Lu DY, Gygi F, Galli G (2008) Dielectric Properties of Ice and Liquid Water from First-Principles Calculations. *Phys. Rev. Lett.* 100:147601.

[41] Pedersen UR, Hummel F, Kresse G, Kahl G, Dellago C (2013) Computing Gibbs Free Energy Differences by Interface Pinning. *Phys. Rev. B* 88:094101.

[42] Pedersen UR (2013) Direct Calculation of the Solid-Liquid Gibbs Free Energy Difference in a Single Equilibrium Simulation. *J. Chem. Phys.* 139:104102.

[43] Saitta AM, Datchi F (2003) Structure and Phase Diagram of High-Density water: The Role of Interstitial Molecules. *Phys. Rev. E* 67:020201.

[44] Brehm M, Kirchner B (2011) TRAVIS - A Free Analyzer and Visualizer for Monte Carlo and Molecular Dynamics Trajectories. *J. Chem. Inf. Model.* 51:2007–2023.

[45] Kroon J, Kanters JA (1974) Nonlinearity of Hydrogen-Bonds In Molecular-Crystals. *Nature* 248:667–669.

[46] Jorgensen WL, Chandrasekhar J, Madura JD, Impey RW, Klein ML (1983) Comparison of Simple Potential Functions for Simulating Liquid Water. *J. Chem. Phys.* 79:926–935.

[47] Berendsen HJC, Grigera JR, Straatsma TP (1987) The Missing Term in Effective Pair Potentials. *J. Phys. Chem.* 91:6269–6271.

[48] Horn HW et al. (2004) Development of an Improved Four-Site Water Model for Biomolecular Simulations: TIP4P-Ew. *J. Chem. Phys.* 120(20):9665–9678.

[49] Abascal JLF, Vega C (2005) A General Purpose Model for the Condensed Phases of Water: TIP4P/2005. *J. Chem. Phys.* 123:234505.

[50] Abascal JLF, Sanz E, Fernandez RG, Vega C (2005) A Potential Model for the Study of Ices and Amorphous Water: TIP4P/Ice. *J. Chem. Phys.* 122:234511.

[51] Vega C, Sanz E, Abascal JLF (2005) The Melting Temperature of the Most Common Models of Water. *J. Chem. Phys.* 122:114507.

[52] Grimme S (2013) DFT-D3 V3.0_Rev2. http://www.thch.uni-bonn.de/tc/?section=downloads.

[53] Imoto S, Forbert H, Marx D (2015) Water structure and solvation of osmolytes at high hydrostatic pressure: pure water and TMAO solutions at 10 kbar versus 1 bar. *Phys. Chem. Chem. Phys.* 17:24224–37.

[54] Xu HF, Stern HA, Berne BJ (2002) Can Water Polarizability be Ignored in Hydrogen Bond Kinetics? *J. Phys. Chem. B* 106:2054–2060.

[55] Kell GS (1975) Density, Thermal Expansivity, and Compressibility of Liquid Water From 0 Degrees To 150 Degreesc - Correlations and Tables For Atmospheric-Pressure and Saturation Reviewed and Expressed On 1968 Temperature Scale. *J. Chem. Eng. Data* 20:97–105.

[56] Haynes WM, ed. (2015) *CRC Handbook of Chemistry and Physics, 95th Edition (Internet Version 2015).* (CRC Press/Taylor and Francis, Boca Raton, FL.).